Electronic structure of the $BaTi_2As_2O$ parent compound of the titanium-based oxypnictide superconductor

H. C. Xu,[1] M. Xu,[1] R. Peng,[1] Y. Zhang,[1] Q. Q. Ge,[1] F. Qin,[1] M. Xia,[1] J. J. Ying,[2] X. H. Chen,[2] X. L. Yu,[3] L. J. Zou,[3] M. Arita,[4] K. Shimada,[4] M. Taniguchi,[4] D. H. Lu,[5] B. P. Xie,[1,*] and D. L. Feng[1,†]

[1]*State Key Laboratory of Surface Physics, Department of Physics, and Advanced Materials Laboratory, Fudan University, Shanghai 200433, People's Republic of China*

[2]*Hefei National Laboratory for Physical Science at Microscale and Department of Physics, University of Science and Technology of China, Hefei, Anhui 230026, People's Republic of China*

[3]*Key Laboratory of Materials Physics, Institute of Solid State Physics, Chinese Academy of Sciences, P. O. Box 1129, Hefei 230031, China*

[4]*Hiroshima Synchrotron Radiation Center and Graduate School of Science, Hiroshima University, Hiroshima 739-8526, Japan*

[5]*Department of Applied Physics and Stanford Synchrotron Radiation Laboratory, Stanford University, Stanford, California 94305, USA*

(Received 28 January 2014; revised manuscript received 23 March 2014; published 8 April 2014)

The electronic structure of $BaTi_2As_2O$, a parent compound of the newly discovered titanium-based oxypnictide superconductors, is studied by angle-resolved photoemission spectroscopy and first-principles calculation. The experimental electronic structure shows a multiorbital nature and three-dimensional character, which is consistent with the calculated results. An anomalous temperature-dependent spectral weight redistribution and broad line shape indicate the incoherent nature of the spectral function. At the density-wave-like transition temperature around 200 K, a partial gap opens at the Fermi patches. These findings suggest that $BaTi_2As_2O$ is likely a charge density wave material in the strong-interaction regime.

DOI: 10.1103/PhysRevB.89.155108 PACS number(s): 71.45.Lr, 75.30.Fv, 74.70.−b, 79.60.Bm

I. INTRODUCTION

The planar square lattice made of 3*d* transition elements and anions has been proven to be a rich playground for high-temperature superconductivity, as exemplified in the CuO_2 plane of the cuprate high-temperature superconductors and the FeAs or FeSe plane of the iron-based superconductors. Recently, superconductivity has been discovered in $Ba_{1-x}Na_xTi_2Sb_2O$ ($0.0 \leqslant x \leqslant 0.33$) [1,2], a titanium-based oxypnictide with an anti-CuO_2 type Ti_2O plane and Sb above and below the center of each Ti_2O square. From the structural point of view, such a lattice is an intriguing combination of both CuO_2 and FeAs types of lattices; thus it may be another family of unconventional superconductors based on titanium, although the maximal T_c is currently only 5.5 K upon Na doping [2].

The signature of possible charge density waves or spin density waves has been observed in $Ba_{1-x}Na_xTi_2Sb_2O$ and other compounds with $(Ti_2Pn_2O)^{2-}$ (Pn = As, Sb) layers [3–7], resembling that in the iron-based high-temperature superconductors. The instability of the ordered state, such as spin fluctuation, often plays an important role in the unconventional superconductivity [8]. Therefore, it is critical to reveal the nature of the density wave transition. Theoretical calculations suggest that the nested Fermi surface sections drive the density wave instability [9–11]. However, the experimental electronic structure of such materials has not been reported. Moreover, density wave order has not been identified in powder neutron diffraction experiments on $Na_2Ti_2Pn_2O$ (Pn = As, Sb) [12,13]. Only recently have the muon spin rotation and nuclear magnetic resonance studies excluded magnetic order in $Ba_{1-x}Na_xTi_2Sb_2O$ and favored a charge density wave picture [14,15].

$BaTi_2As_2O$ is an isostructural compound of the superconducting $BaTi_2Sb_2O$, with isovalent substitution of Sb by As [Fig. 1(a)] [3]. Thus it could be viewed as a parent compound of the titanium-based superconductors. A density wave transition takes place around 200 K, as shown by the resistivity data [Fig. 1(b)]. In this article, we investigate the electronic structure of $BaTi_2As_2O$ with angle-resolved photoemission spectroscopy (ARPES) and first-principles calculation. The photoemission spectra show a broad line shape without a sharp quasiparticle peak near the Fermi energy (E_F). The spectral weight at E_F forms Fermi pockets with parallel sections and Fermi patches (finite spectral weight away from Fermi surfaces). Our polarization and photon energy dependent studies reveal the multiorbital and three-dimensional nature of this material. Intriguingly, the spectral weight redistributes over a large energy scale as a function of temperature, indicating the incoherent nature of the spectral function. Furthermore, a partial gap opens at the Fermi patches around the density wave transition temperature, which is similar to charge density wave materials in the strong-interaction regime [16,17].

II. EXPERIMENTAL AND COMPUTATIONAL DETAILS

Single crystals of $BaTi_2As_2O$ were grown by the flux method [3,18]. The ARPES data were taken at beamline 1 and beamline 9 of the Hiroshima Synchrotron Radiation Center (HiSOR). Temperature-dependent study was conducted at beamline 5-4 of the Stanford Synchrotron Radiation Lightsource (SSRL). The 7 eV laser data were taken with an in-house setup at Fudan University. All data were collected with Scienta R4000 electron analyzers. The energy resolution is 20 meV at HiSOR beamline 1, 10 meV at HiSOR beamline

*bpxie@fudan.edu.cn
†dlfeng@fudan.edu.cn

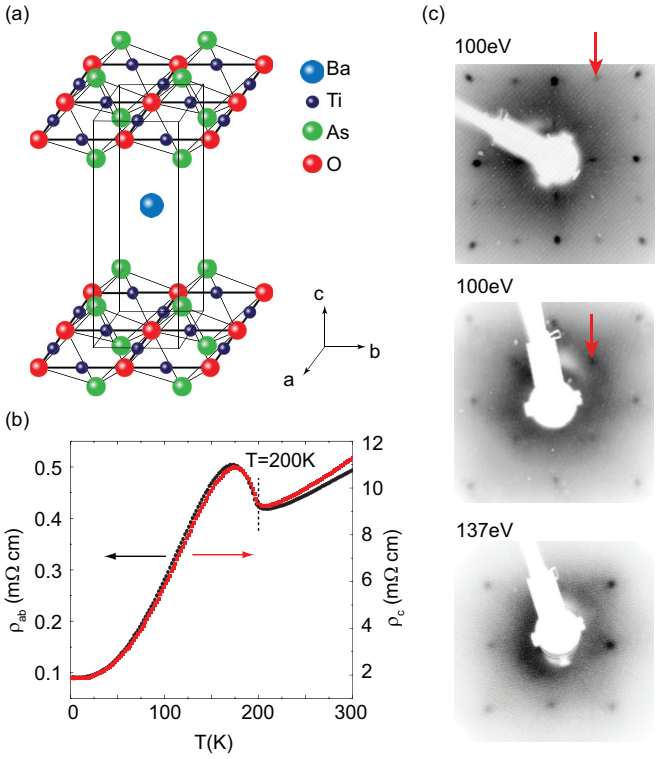

FIG. 1. (Color online) (a) The crystal structure of $BaTi_2As_2O$. (b) In-plane and out-of-plane resistivity as a function of temperature for $BaTi_2As_2O$. (c) The low-energy electron diffraction patterns of three $BaTi_2As_2O$ samples. The arrows mark the reconstruction spots.

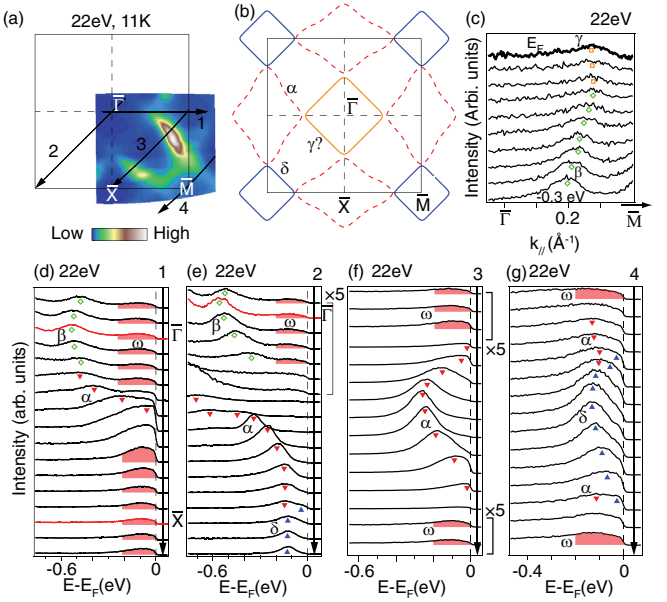

FIG. 2. (Color online) Electronic structure of $BaTi_2As_2O$ measured at 11 K. (a) Photoemission intensity map at the Fermi energy (E_F) integrated over an energy window of ±10 meV. $\bar{\Gamma}$, $\bar{M}$, and $\bar{X}$ stand for high-symmetric points of the projected two-dimensional Brillioun zone (BZ). (b) The Fermi surface sheets obtained by tracking the Fermi crossings in panel (a). The dashed lines indicate the hole pockets, and the solid blue lines indicate the electron pockets. (c) Momentum distribution curves (MDC's) along $\bar{\Gamma}$-$\bar{M}$ near zone center. (d)–(g) Energy distribution curves (EDC's) taken with circular polarized light at 11 K along cuts 1, 2, 3, and 4 in panel (a), respectively. Some parts of the spectra are magnified for a better view.

9, 5 meV at SSRL, and 4 meV for the laser setup. The samples were cleaved *in situ* and measured under ultrahigh vacuum better than 3×10^{-11} mbar. The low-energy electron diffraction (LEED) patterns in Fig. 1(c) indicate the square lattice of a cleaved surface [the *ab* plane in Fig. 1(a)]. Additional surface reconstruction spots, as indicated by the arrows, appear on part of the samples depending on cleavages. These reconstructions probably come from the different rearrangement of the half-layer Ba atoms at the surface similar to those in $BaFe_{2-x}Co_xAs_2$ [19]. For samples with different surface reconstructions, we did not observe significant difference in the electronic structure. The spectra in our paper, if not specified otherwise, represent the general features of $BaTi_2As_2O$. Aging effects were strictly monitored during the experiments.

All the calculations were performed using the standard full-potential linearized augmented plane-wave (FPLAPW) code of the WIEN2K package. The muffin-tin sphere radii were 2.5, 2.02, 2.4, and 1.79 bohrs for Ba, Ti, As, and O atoms, respectively. The cutoff parameter $R_{mt}K_{\max}$ was chosen to be 7.0. The electronic structure was calculated using standard density functional theory based on the Perdew-Barke-Ernzerhof generalized gradient approximation (GGA) [20]. The number of **k** points was 2000 for unit cell and 1000 for supercell with the application of symmetry groups.

III. BAND STRUCTURE

Figure 2(a) shows the photoemission intensity map of $BaTi_2As_2O$ at E_F. As sketched in Fig. 2(b), the Fermi surfaces in the projected two-dimensional Brillioun zone (BZ) consists of four diamond-shaped hole pockets (α) centered at four $\bar{X}$ points, four square-shaped electron pockets (δ) centered at four $\bar{M}$ points, and one square-shaped pocket (γ) centered at $\bar{\Gamma}$. At first glance, the Fermi surfaces may come from the warping and hybridization of two sets of quasi-1D sections along (1,1) and (−1,1) directions [9]. In this case, there should be an electron pocket at the zone center. Indeed, an electron-like band β is observed below E_F around $\bar{\Gamma}$ [Figs. 2(c)–2(e)]. However, the features become weak and vague as approaching E_F, while the band γ appears and crosses E_F with nearly vertical dispersion near the zone center [Fig. 2(c)]. We cannot tell whether the band γ is electron-like or hole-like from the 22 eV data. The square-shaped pockets at $\bar{M}$ and $\bar{\Gamma}$ show multiple parallel sections, providing possible Fermi surface nesting condition for density wave instabilities, as suggested in previous theoretical calculations [8–11].

Figure 2(d) shows the energy distribution curves (EDC's) along $\bar{\Gamma}$-$\bar{X}$, crossing $\bar{\Gamma}$, and the pockets centered at $\bar{X}$ [cut 1 in Fig. 2(a)]. Band α contributes prominent spectral weight and forms the hole pocket around $\bar{X}$. Along cut 2, band α disperses towards E_F and coincides with the bottom of band δ, which forms the electron pocket at zone corner [Fig. 2(e)]. Bands α and δ keep a broad line shape while approaching E_F, and cross E_F without a sharp quasiparticle peak. Along both cuts 1 and 2, band β is observed below E_F near zone center

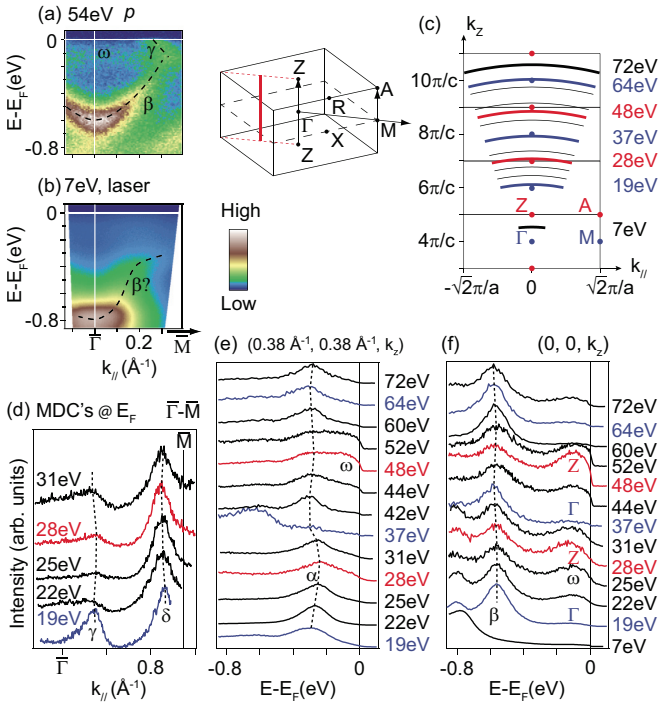

FIG. 3. (Color online) (a) Spectral intensity along $\bar{\Gamma}$-$\bar{M}$ near zone center. (b) The same as panel (a), but taken with 7 eV laser. (c) Sketch of BZ's in Γ-M-A-Z plane. The corresponding positions for different photon energies are indicated, with the inner potential assumed to be 12 eV. The inset illustrates the three-dimensional BZ of $BaTi_2As_2O$. (d) MDC's at E_F along $\bar{\Gamma}$-$\bar{M}$ as a function of photon energy. (e) EDC's taken along (0.38 $Å^{-1}$, 0.38 $Å^{-1}$, k_z) (the red solid line in the three-dimensional BZ) with various photon energies as shown in panel (c). (f) The same as panel (e), but along (0, 0, k_z).

[Figs. 2(d) and 2(e)], while band γ, which forms the pocket at $\bar{\Gamma}$, could hardly be tracked in EDC's due to its weak intensity and nearly vertical dispersion [Fig. 2(c)]. Figure 2(f) shows the dispersion of band α along cut 3 between two neighboring hole pockets. In Fig. 2(g), bands α and δ along cut 4 show similar dispersive structures with those near zone corner along cut 2. Moreover, in Figs. 2(d)–2(g), there is spectral weight with broad line shape (shaded area) between −0.2 eV and E_F, labeled as ω, contributing finite spectral weight over almost the entire BZ.

The band dispersion along k_z was investigated by photon energy dependent study. In the spectra taken with 54 eV photons [Fig. 3(a)], the electron-like band β is observed below E_F, while the band γ appears hole-like and crosses E_F near the zone center. Figure 3(b) shows the photoemission spectra taken with a 7 eV laser, which is featureless near E_F. The distinct band structure implies strong dispersion along k_z, consistent with the previous band calculations [8,10,11,21]. We have performed a detailed study with photon energies ranging from 19 to 72 eV, covering more than two BZ's along k_z [Fig. 3(c)]. The dispersions of bands γ, δ [Fig. 3(d)], and α [Fig. 3(e)] match the period of BZ along k_z if assuming the inner potential to be 12 eV. Moreover, the broad feature ω shows a variation of intensity that matches the period of BZ [Figs. 3(e) and 3(f)]. On the other hand, as shown in Figs. 3(d)–3(f), the dispersion is rather weak above 19 eV. Such a weak dispersion along k_z contradicts the distinct spectra taken with the 7 eV laser, suggesting a loss of dispersive information along k_z probably due to the poor k_z resolution for the photon energy range [19 eV, 72 eV]. In the universal curve of escaping depth vs kinetic energy, the mean escaping depth ξ of the photoelectron excited by photons at this energy range is around 7 Å [22], yielding a $\Delta k_z \approx 2\pi/\xi$ as large as the BZ size. This would largely smear out the dispersive information along k_z and result in a weak dispersion and/or Fermi patches, as indeed observed in our data. The escaping depth increases rapidly with photon energies from 19 eV to 7 eV by more than three times [22], providing a much better k_z resolution, which could explain the distinct spectra taken with the 7 eV laser. Intriguingly, the spectra taken with 7 eV photon energy still show intrinsic broad features.

In Fig. 4(a), we compare the experimental band structure, which represents the averaged band dispersion of spectra taken with photon energy from 19 eV to 72 eV in the projected two-dimensional BZ, with the calculated band structure. In the Γ-X-M plane along Γ-M, a hole band (orange curves) and an electron band (green curves) roughly match the dispersion of band γ (orange squares) and band β (green diamonds), respectively. One band shown as red curves along Γ-M corresponds to band α (red inverted triangles), but locates at

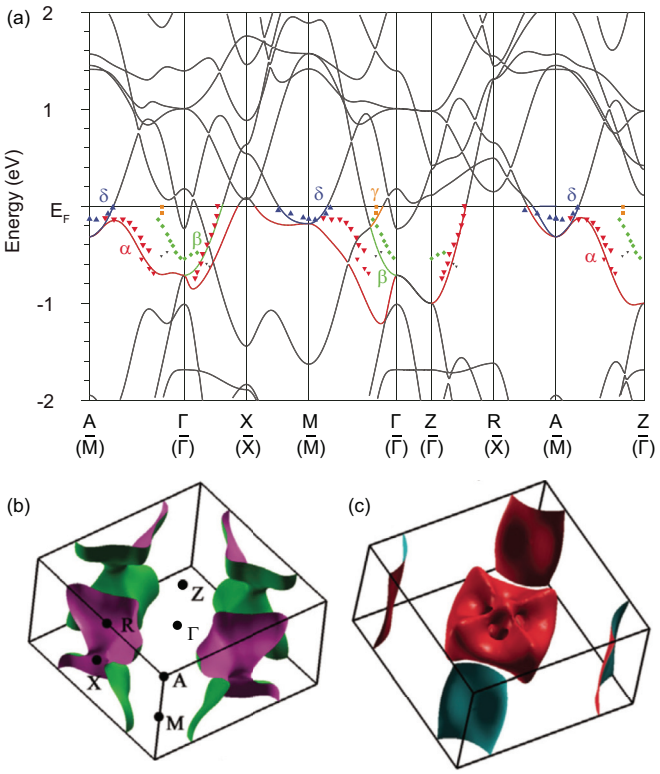

FIG. 4. (Color online) (a) The calculated band structure of $BaTi_2As_2O$. The summarized dispersions from photoemission data for α (red inverted triangles), β (green diamonds), γ (orange squares), and δ (blue triangles) are plotted for comparison. The high-symmetric points in projected two-dimensional BZ corresponding to the experimental data are indicated along the horizontal axis. (b) Hole Fermi surface sheets from calculation. (c) Electron Fermi surface sheets from calculation.

higher binding energies. Along both Γ-M and M-X, the bands in the blue well match the dispersion of band δ (blue triangles). In the Z-R-A plane, the calculated band structure shows significant difference from that in the Γ-X-M plane, which implies strong band dispersion along k_z. Multiple bands around the zone center near E_F, including bands β and γ, disappear around Z. The band α appears at lower binding energies and shows good correspondence with the experimental data along both Z-R and Z-A. Around A, band δ shows Fermi crossings similar to those around M, but its band bottom locates at much higher binding energy.

Figures 4(b) and 4(c) show the calculated Fermi surface sheets [21]. There are four hole Fermi surface sheets at X-R, four electron-type Fermi surface sheets at M-A (zone corner), and one electron-type Fermi surface at Γ. The calculated hole pockets in the Z-R-A plane and electron pockets at zone corner well match the α pockets and δ pockets in our data, respectively. The calculated electron-type Fermi surface sheet at Γ presents a complicated mesh structure in a narrow range along k_z, which is formed by the multiple bands highly dispersive along k_z around Γ in Fig. 4(a). These bands are hard to resolve in our photoemission data due to poor k_z resolution. Under large k_z broadening, the remnants of dispersive bands near E_F could be an origin of the broad feature ω near $\bar{\Gamma}$. Moreover, it is likely that the photoemission with the 7 eV laser, which corresponds to momenta away from Γ [Fig. 3(c)], has missed the electron-type Fermi surface sheet at Γ and leads to a spectra with no dispersive feature near E_F [Fig. 3(b)].

These support that our photoemission data are mainly contributed by the bands β, γ, and δ in the Γ-X-M plane and band α in the Z-R-A plane, where the experimental electronic structure well matches the calculation. The band dispersion from photoemission data shows negligible bandwidth renormalization from the calculated results. On the other hand, the intrinsic broad line shape and the Fermi patches over the BZ resemble those observed in 2H-Na_xTaS_2 before [16], which is a charge density wave material with strong electron-phonon interactions.

IV. MULTIORBITAL NATURE OF BANDS NEAR E_F

For compounds with $(Ti_2Pn_2O)^{2-}$ (Pn = As, Sb) layers, the density of states near E_F is dominated by Ti 3*d* electrons according to theoretical calculations [8,10,11,21], and there is only one 3*d* electron for each Ti^{3+} ion. However, our data show multiple bands crossing E_F in $BaTi_2As_2O$, suggesting multiorbital composition of these bands. In order to reveal the orbital composition of bands near E_F, we calculate the orbital composition as plotted in Fig. 5 in the "fat-band" scheme [8], and check these results with polarization-dependent ARPES study in both *p* and *s* geometries.

Figure 6(a) shows the geometries of the photoemission experiment setup, where the path of the incident photon beam and the sample surface normal define the mirror plane. The matrix element of photoemission could be described by

$$\left|M_{f,i}^{\mathbf{k}}\right|^2 = \left|\langle\phi_f^{\mathbf{k}}|\varepsilon\cdot\mathbf{r}|\phi_i^{\mathbf{k}}\rangle\right|^2,$$

where the $\phi_f^{\mathbf{k}}$ and $\phi_i^{\mathbf{k}}$ are final and initial states, respectively [23]. Given that the final state is a plane wave and its symmetry

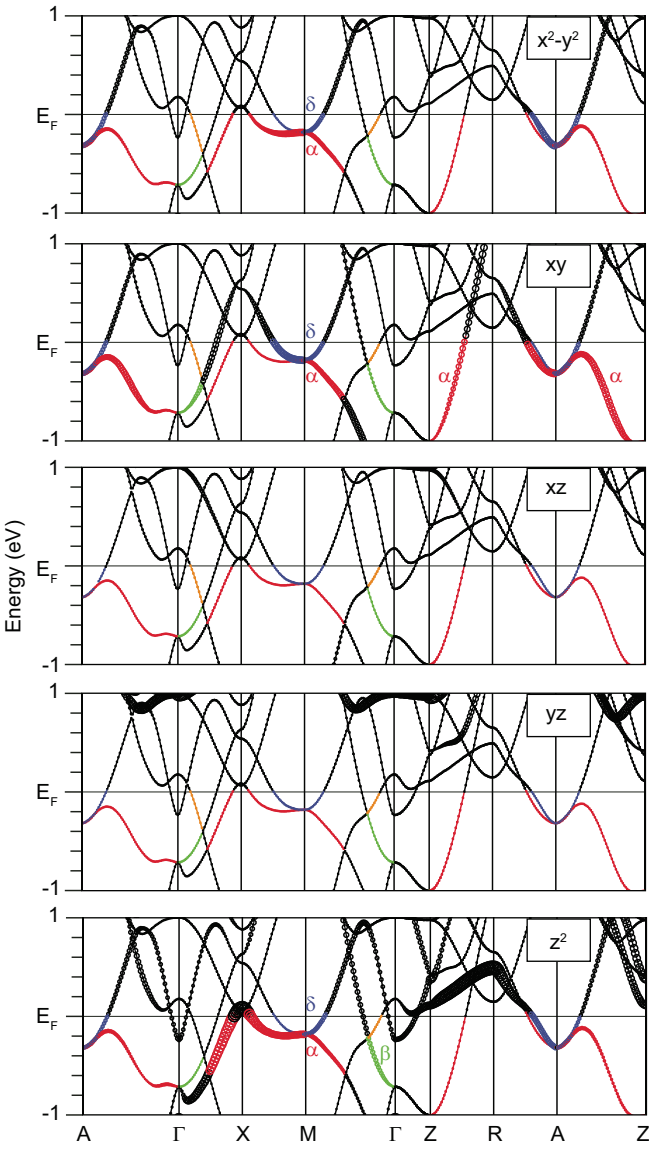

FIG. 5. (Color online) Fat-band plot for different *d* orbital characters near E_F. The *x* axis and *y* axis are defined along the Ti-As-Ti directions. The red, green, orange, and blue curves correspond to bands α, β, γ, and δ, respectively.

is always even against the mirror plane, the photoemission intensity would be suppressed if the initial state and the $(\hat{\varepsilon}\cdot\mathbf{r})$ have opposite symmetries. With the k_x and k_y directions in Fig. 6(b) defined as the Ti-As-Ti direction, the five *d* orbitals are classified into even and odd symmetries in Fig. 6(c) with respect to the Γ-X-R-Z plane. The symmetries with respect to the Γ-M-A-Z plane are indicated in red [Fig. 6(c)]. In the current experimental setup, the even (odd) orbitals should be visible in *p* (*s*) geometry [Fig. 6(c)]. In addition, for the out-of-plane component of the *p*-polarized light, the signal of orbitals extending out-of-plane would be enhanced in this geometry.

As illustrated in Fig. 6(b), polarization-dependent ARPES study around $\bar{\Gamma}$ was conducted along both $\bar{\Gamma}$-$\bar{X}$ (cut 1) and $\bar{\Gamma}$-$\bar{M}$ (cut 2) with 48 eV photons. In Fig. 6(d), some weak features folded from bands α and β show up around $\bar{X}$ (noted as α' and β'), consistent with the surface reconstruction in

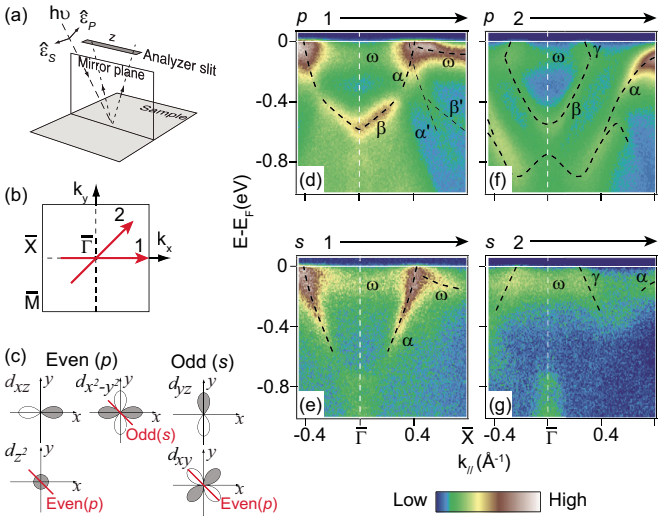

FIG. 6. (Color online) (a) Experimental setup for polarization-dependent ARPES. (b) The sketch of BZ and cuts. (c) The 3*d* orbitals are classified into even and odd symmetries with respect to the Γ-X-R-Z plane. The spatial symmetries with respect to the Γ-M-A-Z plane are illustrated in red color. The geometries indicated in the parentheses provide finite photoemission intensity. (d), (e) Photoemission intensity along cut 1 taken with 48 eV photon energy in *s*-polarized geometry, and in *p*-polarized geometry, respectively. (f), (g) The same as panels (d) and (e), but taken along cut 2.

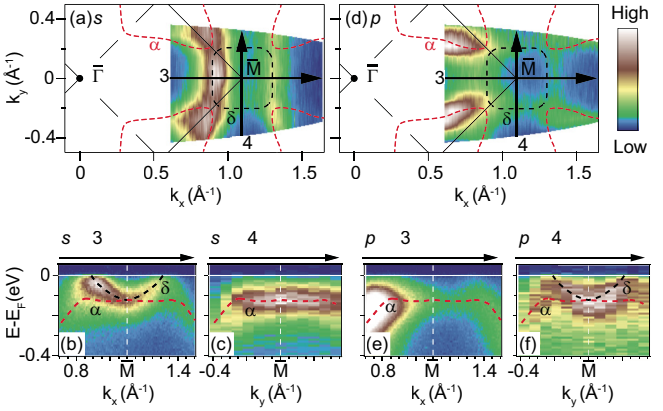

FIG. 7. (Color online) (a) The photoemission intensity map around $\bar{M}$ taken with 22 eV photon energy in *s*-polarized geometry. (b), (c) The photoemission intensity along cuts 3 and 4 in panel (a), respectively. (d), (f) The same as panels (a)–(c), but taken with *p*-polarized geometry. The spectra along cut 4 are generated by combining individual EDC's at corresponding momenta.

the upper panel of Fig. 1(c). In Figs. 6(d) and 6(e), the band α is more clear in *s* geometry along $\bar{\Gamma}$-$\bar{X}$, indicating its odd orbital dominated composition. Along Z-R in the calculated results, where better coincidence with experiment is found for band α, the dominant composition of band α is d_{xy} (see the xy projection in Fig. 5), which is odd with respect to the Γ-X-R-Z plane. The spectral weight of feature ω is enhanced near $\bar{X}$ in *p* geometry, indicating an orbital with even symmetry or an out-of-plane component. Indeed, the calculation shows d_{z^2} composition near E_F around X (see the z^2 projection in Fig. 5), which is even with respect to the Γ-X-R-Z plane. At other momenta, ω is visible in both geometries, suggesting mixed orbital composition.

Along $\bar{\Gamma}$-$\bar{M}$, the band α is visible in *p* geometry [Fig. 6(f)] and suppressed in *s* geometry [Fig. 6(g)], suggesting its even composition along this direction. Consistently, the band α is mainly composed of orbital d_{xy} along Z-A according to the calculation (see the xy projection in Fig. 5), which is even with respect to the Γ-M-A-Z plane. In Figs. 6(f) and 6(g), band γ and ω are visible in both geometries, indicating their mixed orbital composition. Band β and other features at higher binding energies show even symmetry in both $\bar{\Gamma}$-$\bar{X}$ and $\bar{\Gamma}$-$\bar{M}$ direction [Figs. 6(d)–6(g)]. Consistently, the calculation shows d_{xy} composition along Γ-X and d_{z^2} composition along Γ-M for band β (see the xy and z^2 projections in Fig. 5). Both d_{xy} and d_{z^2} are even with respect to the the Γ-M-A-Z plane and the Γ-X-R-Z plane, respectively.

As shown by the Fermi surface mapping in *s* geometry [Fig. 7(a)], the top and bottom edges of the δ pocket are suppressed, while its left and right edges are fairly intensive. Below E_F in *s* geometry, the band δ is visible along cut 3 but not visible along cut 4 [Figs. 7(b) and 7(c)]. In *p* geometry, the band δ is not visible along cut 3 but visible along cut 4 [Figs. 7(e) and 7(f)]. This suggests that the orbital composition of band δ is odd along cut 3 and even along cut 4, i.e., a switch of orbital symmetries under fourfold rotation about $\bar{M}$. In the calculated results along Γ-M, the orbital composition of band δ shows a similar amount of $d_{x^2-y^2}$, d_{xy}, and d_{z^2} (Fig. 5). The hybridization of these orbitals could explain the complicated polarization dependence of band δ in the photoemission data.

Around $\bar{M}$, band α shows flat dispersion and is visible in both geometries and along both cuts 3 and 4 [Figs. 7(b)–7(c) and 7(e)–7(f)], indicating mixed orbital composition. A change of orbital composition between the dispersive part and the flat part could be observed from the intensity change of band α in Figs. 7(c) and 7(e). As demonstrated before, the dispersive part of band α corresponds to the calculated band along Z-A, where the d_{xy} orbital dominates. In contrast, the flat part of band α matches the calculated bands around M better, where it shows mixed orbital composition including $d_{x^2-y^2}$ and d_{z^2} besides d_{xy}.

Our calculation and experimental results on $BaTi_2As_2O$ show that the features near E_F come from the hybridization of multiple Ti 3*d* orbitals, and demonstrate the multiorbital composition of the bands near E_F. The multiorbital character in $BaTi_2As_2O$ resembles that in the iron-based superconductors [24–26].

V. TEMPERATURE-DEPENDENT STUDY

Now we turn to the temperature-dependent study on the density wave transition in $BaTi_2As_2O$. In the conventional picture of density wave transition, a gap opens along parallel Fermi surface sheets when the system enters the density wave state [8,10,11]. Considering the Fermi patches spreading over the BZ and the lack of sharp Fermi crossings, we investigated the temperature dependence over a quarter of the BZ. Figure 8(a) shows the false-color map of the spectral weight suppression ratio at E_F from 220 K to 11 K, i.e.,

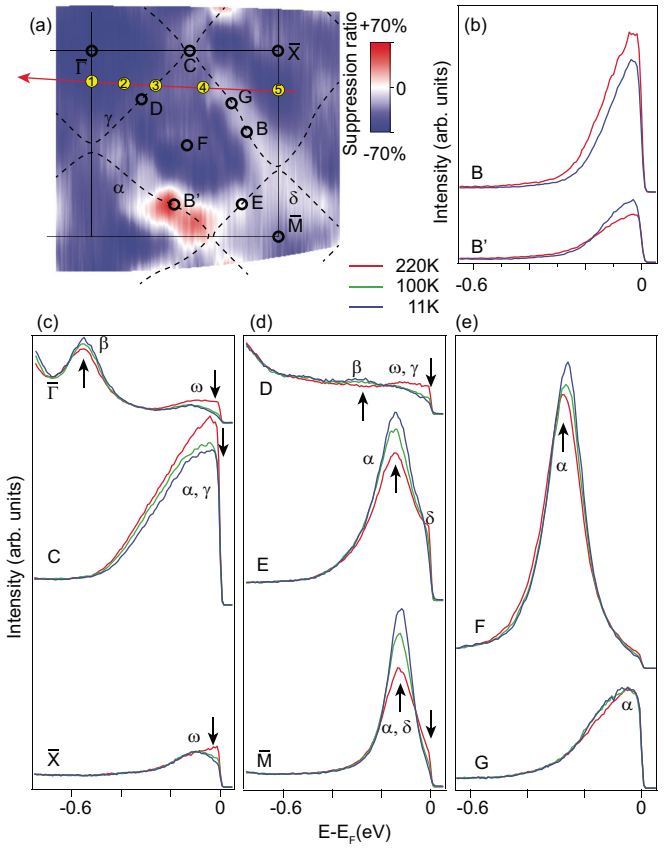

FIG. 8. (Color online) (a) The false-color plot of the spectral weight suppression ratio from 220 K to 11 K, i.e., $[I_{E_F}(11\text{ K}) - I_{E_F}(220\text{ K})]/I_{E_F}(220\text{ K})$. The spectra are integrated over $[E_F - 25\text{ meV}, E_F + 5\text{ meV}]$ after dividing the resolution-convolved Fermi-Dirac function. (b)–(e) Temperature dependence of EDC's at various momenta as marked in panel (a). The thermal broadening near E_F are removed by dividing the spectra with resolution-convolved Fermi-Dirac function at corresponding temperatures and then multiplied by that of 11 K, i.e., $I(E,k,T)/\tilde{f}_{\text{FD}}(E,T)\times\tilde{f}_{\text{FD}}(E,11\text{ K})$, while $\tilde{f}_{\text{FD}}(E,T)$ stands for the resolution-convolved Fermi-Dirac function. The panels (a) and (b) are from the same data set, while the panels (c)–(e) are from individual temperature-dependent studies along fixed momentum cuts. Photoemission data were taken with 22 eV photons.

$[I_{E_F}(11\text{ K}) - I_{E_F}(220\text{ K})]/I_{E_F}(220\text{ K})$. The spectral weight is suppressed at the Fermi patches away from Fermi crossings, where the broad feature ω dominates. The parallel Fermi surface sheets formed by bands γ and δ, where density wave instability was suggested, do not show prominent suppression. Most parts of the α pocket show weak suppression, while one branch at the lower side of BZ shows great enhancement, as exemplified by comparing the temperature dependence of EDC's at momenta B and B′ [Fig. 8(b)]. The partial suppression of spectral weight at E_F is consistent with the metallic behavior below transition [Fig. 1(b)], and agrees with previous optical study on its sibling material $Na_2Ti_2As_2O$ [27]. However, such an asymmetric suppression/enhancement for the α pocket cannot be explained by the matrix element effect, possibly due to other momentum-dependent effects.

Figures 8(c)–8(e) show the EDC's at various momenta as marked in Fig. 8(a). The EDC's are divided by the resolution-convolved Fermi-Dirac function at corresponding temperature and multiplied by that of 11 K to remove thermal broadening effects near E_F. The suppression of spectral weight takes place near E_F, as indicated by the down arrows on the EDC's for momenta $\bar{\Gamma}$, C, $\bar{\text{X}}$ [Fig. 8(c)], D, and $\bar{\text{M}}$ [Fig. 8(d)]. On the other hand, the spectral weight of bands α, β, and δ below E_F enhances with decreasing temperature [up arrows in Figs. 8(c)–8(e)]. Thus the evolution of spectral weight distribution with temperature could be viewed as a spectral weight redistribution from Fermi patches at E_F to the dispersive bands at higher binding energies, which saves energy. The energy scale of the spectral weight redistribution ranges from 0.1 eV for bands α/δ at zone corner, to 0.6 eV for band β at zone center, which is far beyond the energy range of thermal effect and is not expected in a noninteracting electron system. The spectral weight enhancement for bands α, β, and δ do not slow down below 100 K [up arrows in Figs. 8(c)–8(e)], indicating that it is not relevant to the density wave transition around 200 K. Similar large-scale spectral weight redistribution was observed in $Sr_2CuO_2Cl_2$, which is explained by multiple initial/final states induced by strong coupling between electrons and bosons [28]. The large-scale spectral weight redistribution in $BaTi_2As_2O$ could originate from a similar strong-coupling effect, which is probably momentum dependent and induces an asymmetric suppression/enhancement as observed in Fig. 8(a). On the other hand, the spectral weight suppression at E_F mostly takes place between 220 K and 100 K [down arrows in Figs. 8(c)–8(e)], suggesting a density wave transition related component.

In order to investigate the density wave transition related component, we conduct detailed temperature-dependent study around 200 K along the cut through momenta ①∼⑤ as marked in Fig. 8(a). This cut is selected to cover momenta ① and ② (the Fermi patch inside the Fermi surface γ), momentum ⑤ (the Fermi patch inside the Fermi surface α), and momentum ④ (the Fermi patch between the Fermi surfaces), while the bands α and β are resolved [Fig. 9(a)]. Figure 9(b) shows the spectral weight difference between 236 K and 168 K. The major suppression of spectral weight takes place around E_F, while the enhancement is mainly at higher binding energies on bands α and β, demonstrating the spectral weight redistribution. Detailed temperature evolutions of relative spectral weight at momenta ① ∼ ⑤ are plotted in Figs. 9(c) and 9(d), for energy windows $[E_F - 25\text{ meV}, E_F + 5\text{ meV}]$ ($R^{E_F+5}_{E_F-25}$) and $[E_F - 200\text{ meV}, E_F - 50\text{ meV}]$ ($R^{E_F-50}_{E_F-200}$), respectively. At most momenta and binding energies, the spectral weight show smooth suppression/enhancement though 200 K, demonstrating the spectral weight redistribution independent of the density wave transition. On the other hand, slope changes are observed around 200 K for momenta ④ and ⑤ [Fig. 9(c)], indicating gap opening of density wave transition at these momentum. At momentum ②, after dividing the temperature-dependent curve of $R^{E_F+5}_{E_F-25}$ by that of $R^{E_F-50}_{E_F-200}$, both of which show smooth evolution, a slope change around 200 K is readily observable [$R^{E_F+5}_{E_F-25}/R^{E_F-50}_{E_F-200}$ in Fig. 9(e)], demonstrating a partial gap opening buried under the large spectral weight redistribution. Note that the density wave transition related slope changes take place at Fermi patches (e.g., momenta ②, ④, and ⑤) without well-defined Fermi surfaces, suggesting that the partial gap opening takes place at

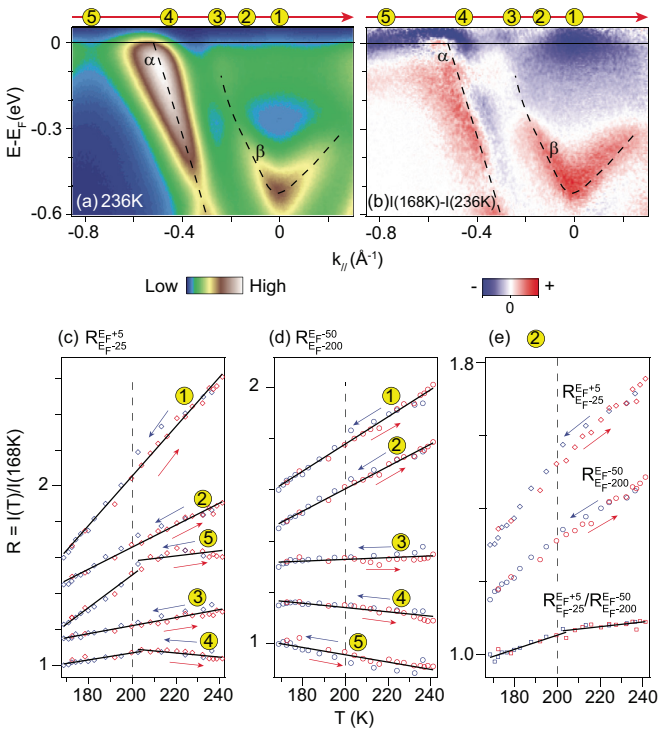

FIG. 9. (Color online) (a) Photoemission spectra taken at 236 K with 22 eV photons along cuts ①–⑤, as marked in Fig. 8(a). (b) The difference between the spectra at 236 K and 168 K, which are divided by the resolution-convoluted Fermi-Dirac distributions at the corresponding temperatures before subtraction. (c) Density of states as a function of temperature normalized by that at 168 K, integrated over $[E_F - 25$ meV, $E_F + 5$ meV$]$ $(R^{E_F+5}_{E_F-25})$ at corresponding momenta ①–⑤. The blue data points and arrows indicate process of decreasing temperature, while the red ones stand for increasing temperature. (d) The same as panel (c), but integrated over $[E_F - 200$ meV, $E_F - 50$ meV$]$ $(R^{E_F-50}_{E_F-200})$. (f) $R^{E_F+5}_{E_F-25}$, $R^{E_F-50}_{E_F-200}$ at momentum ②, and their ratio $(R^{E_F+5}_{E_F-25}/R^{E_F-50}_{E_F-200})$ as a function of temperature. The data in (c)–(e) are vertically offset for a better view.

Fermi patches, rather than at the nested Fermi surface sections based on the conventional density wave picture [8,10,11].

VI. DISCUSSION AND CONCLUSION

The dispersive features in photoemission spectra of $BaTi_2As_2O$ show a broad line shape and cross E_F without sharp quasiparticle peaks. On the other hand, the overall bandwidth shows little renormalization compared with the calculated band structure [Fig. 4(a)]. These characters resemble those in polaronic systems such as $La_{1.2}Sr_{1.8}Mn_2O_7$, where incoherent broad features dominate the photoemission spectra with vanishingly small quasiparticle weight, while following the bare band dispersion [29,30]. The polaronic picture is further supported by the large-scale temperature-dependent spectral weight redistribution, which resembles that in $Sr_2CuO_2Cl_2$ induced by strong electron correlations with phonons or magnetic excitations [28].

Due to the interference of large-scale temperature-dependent spectral weight redistribution, it is hard to extract the exact momentum distribution of density wave gap opening. However, the signature of partial gap opening on Fermi patches rather than Fermi surfaces provides some clue for further investigation. Since the Fermi patches partly come from the convolving of highly k_z-dispersive bands, an out-of-plane nesting vector could be expected to form the density wave instability, like that in VSe_2 [31]. On the other hand, charge density wave instabilities formed by Fermi patches or barely occupied states were reported in 2H-Na_xTaS_2 and $NbSe_2$ [16,17], which show polaronic signatures. Therefore, $BaTi_2As_2O$ is likely a similar charge density wave material in the strong-interaction regime. Moreover, considering the conventional s-wave superconductivity in 2H-Na_xTaS_2 and $NbSe_2$ and recent reports [14,15,32], the superconductivity in titanium oxypnictides could also be conventional.

In summary, we have carried out a systematic ARPES and first-principles study on $BaTi_2As_2O$ and revealed its band structure with a multiorbital nature and three-dimensional character. The spectral weight at E_F forms both Fermi surfaces and Fermi patches. The broad line shape and anomalous temperature dependence of spectral weight redistribution suggest the incoherent nature of the spectral functions due to strong interactions. Partial gap openings at the transition temperature are observed on Fermi patches rather than the parallel sections of Fermi surfaces, which resembles charge density wave materials in the strong-interaction regime.

ACKNOWLEDGMENTS

We gratefully acknowledge helpful discussions with Prof. J. P. Hu. This work is supported in part by the National Science Foundation of China and the National Basic Research Program of China (973 Program) under Grants No. 2012CB921400, No. 2011CB921802, No. 2011CBA00112, No. 2011CB309703, and No. 91026016. SSRL is operated by the US DOE, BES, Divisions of Chemical Sciences and Material Sciences.

[1] T. Yajima, K. Nakano, F. Takeiri, T. Ono, Y. Hosokoshi, Y. Matsushita, J. Heister, Y. Kobayashi, and H. Kageyama, J. Phys. Soc. Jpn. **81**, 103706 (2012).

[2] P. Doan, M. Gooch, Z. Tang, B. Lorenz, A. Moeller, J. Tapp, P. C. W. Chu, and A. M. Guloy, J. Am. Chem. Soc. **134**, 16520 (2012).

[3] X. F. Wang, Y. J. Yan, J. J. Ying, Q. J. Li, M. Zhang, N. Xu, and X. H. Chen, J. Phys.: Condens. Matter **22**, 075702 (2010).

[4] E. A. Axtell III, T. Ozawa, S. M. Kauzlarich, and R. R. P. Singh, J. Solid State Chem. **134**, 423 (1997).

[5] T. C. Ozawa and S. M. Kauzlarich, J. of Cryst. Growth **265**, 571 (2004).

[6] R. H. Liu, D. Tan, Y. A. Song, Q. J. Li, Y. J. Yan, J. J. Ying, Y. L. Xie, X. F. Wang, and X. H. Chen, Phys. Rev. B **80**, 144516 (2009).
[7] R. H. Liu, Y. A. Song, Q. J. Li, J. J. Ying, Y. J. Yan, Y. He, and X. H. Chen, Chem. Mater. **22**, 1503 (2010).
[8] D. J. Singh, New J. Phys. **14**, 123003 (2012).
[9] F. F. Biani, P. Alemany, and E. Canadell, Inorg. Chem. **37**, 5807 (1998).
[10] W. E. Pickett, Phys. Rev. B **58**, 4335 (1998).
[11] X. W. Yan and Z. Y. Lu, J. Phys.: Condens. Matter **25**, 365501 (2013).
[12] T. C. Ozawa, R. Pantoja, E. A. Axtell, III, S. M. Kauzlarich, J. E. Greedan, M. Bieringer, and J. W. Richardson, Jr., J. Solid State Chem. **153**, 275 (2000).
[13] T. C. Ozawa, S. M. Kauzlarich, M. Bieringer, and J. E. Greedan, Chem. Mater. **13**, 1804 (2001).
[14] S. Kitagawa, K. Ishida, K. Nakano, T. Yajima, and H. Kageyama, Phys. Rev. B **87**, 060510 (2013).
[15] F. von Rohr, A. Schilling, R. Nesper, C. Baines, and M. Bendele, Phys. Rev. B **88**, 140501 (2013).
[16] D. W. Shen, B. P. Xie, J. F. Zhao, L. X. Yang, L. Fang, J. Shi, R. H. He, D. H. Lu, H. H. Wen, and D. L. Feng, Phys. Rev. Lett. **99**, 216404 (2007).
[17] D. W. Shen, Y. Zhang, L. X. Yang, J. Wei, H. W. Ou, J. K. Dong, B. P. Xie, C. He, J. F. Zhao, B. Zhou, M. Arita, K. Shimada, H. Namatame, M. Taniguchi, J. Shi, and D. L. Feng, Phys. Rev. Lett. **101**, 226406 (2008).
[18] X. F. Wang, T. Wu, G. Wu, H. Chen, Y. L. Xie, J. J. Ying, Y. J. Yan, R. H. Liu, and X. H. Chen, Phys. Rev. Lett. **102**, 117005 (2009).
[19] F. Massee, S. de Jong, Y. Huang, J. Kaas, E. van Heumen, J. B. Goedkoop, and M. S. Golden, Phys. Rev. B **80**, 140507 (2009).
[20] J. P. Perdew, K. Burke, and M. Ernzerhof, Phys. Rev. Lett. **77**, 3865 (1996).
[21] Xiang-Long Yu, Da-Yong Liu, Ya-Min Quan, Ting Jia, Hai-Qing Lin, and Liang-Jian Zou, J. Appl. Phys. **115**, 17A924 (2014).
[22] S. Hüfner, *Photoelectron Spectroscopy: Principles and Application* (Springer-Verlag, New York, 1995).
[23] A. Damascelli, Z. Hussain, and Z.-X. Shen, Rev. Mod. Phys. **75**, 473 (2003).
[24] K. Kuroki, S. Onari, R. Arita, H. Usui, Y. Tanaka, H. Kontani, and H. Aoki, Phys. Rev. Lett. **101**, 087004 (2008).
[25] S. Graser, T. A. Maier, P. J. Hirschfeld, and D. J. Scalapino, New J. Phys. **11**, 025016 (2009).
[26] D. J. Singh and M. H. Du, Phys. Rev. Lett. **100**, 237003 (2008).
[27] Y. Huang, H. P. Wang, W. D. Wang, Y. G. Shi, and N. L. Wang, Phys. Rev. B **87**, 100507 (2013).
[28] C. Kim, F. Ronning, A. Damascelli, D. L. Feng, Z.-X. Shen, B. O. Wells, Y. J. Kim, R. J. Birgeneau, M. A. Kastner, L. L. Miller, H. Eisaki, and S. Uchida, Phys. Rev. B **65**, 174516 (2002).
[29] N. Mannella, W. L. Yang, X. J. Zhou, H. Zheng, J. F. Mitchell, J. Zaanen, T. P. Devereaux, N. Nagaosa, Z. Hussain, and Z.-X. Shen, Nature (London) **438**, 474 (2005).
[30] D. S. Dessau, T. Saitoh, C.-H. Park, Z.-X. Shen, P. Villella, N. Hamada, Y. Moritomo, and Y. Tokura, Phys. Rev. Lett. **81**, 192 (1998).
[31] V. N. Strocov, M. Shi, M. Kobayashi, C. Monney, X. Wang, J. Krempasky, T. Schmitt, L. Patthey, H. Berger, and P. Blaha, Phys. Rev. Lett. **109**, 086401 (2012).
[32] A. Subedi, Phys. Rev. B **87**, 054506 (2013).